Combinatorial design of amorphous TaNiSiC thin films with enhanced hardness, thermal stability, and corrosion resistance

Maciej Kaplan [a],[*],[1], Aishwarya Srinath [b],[1], Lars Riekehr [b], Leif Nyholm [b], Björgvin Hjörvarsson [a], Stefan Fritze [b]

[a] Materials Physics, Department of Physics and Astronomy, Uppsala University, Sweden
[b] Department of Chemistry – Ångström Laboratory, Uppsala University, Sweden

HIGHLIGHTS

- The peak hardness of the as-grown films was 12.4 GPa and increased 4 GPa after annealing.
- The TaNiSiC remained amorphous after annealing up to 700 °C for a total of four hours.
- A few atomic percent of Si significantly increased the corrosion resistance.
- Separation of Ni and C decrease the resistance to crystallization and material properties.

GRAPHICAL ABSTRACT
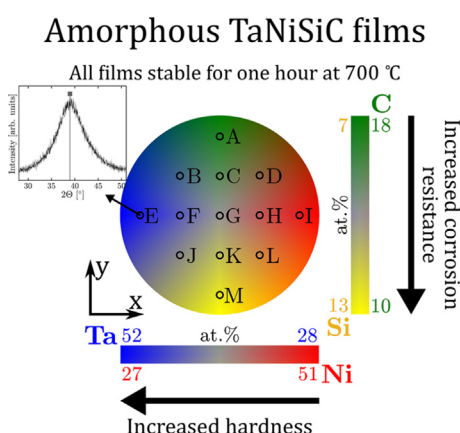
ARTICLE INFO

ABSTRACT

Amorphous TaNiSiC and TaNiC films (with varying Ta/Ni and Si/C ratios) were deposited using combinatorial magnetron sputtering. The TaNiSiC films remained X-ray amorphous after four hour-long annealings up to 700 °C, while TaNiC alloys with high Ni and C contents crystallized. These differences were attributed to a strong driving force for separation of Ni and C in TaNiC, whereas the addition of Si, due to its solubility in the other elements, reduced the elemental segregation in TaNiSiC. The as-deposited TaNiSiC films exhibited hardnesses of 9–12 GPa. Annealing led to an increase in hardness by 2–4 GPa, due to decreases in average atomic distance, as evidenced by X-ray diffraction measurements. Potentiodynamic polarizations from –0.7 to +1.5 V vs. Ag/AgCl (3 M NaCl) in 10 mM sodium borate showed lower current densities by up to 2 orders of magnitude with increasing Ta content (28–52 at. %). Changes in Si/C content (7–13 at.% Si) had no effect. However, optical microscopy showed that TaNiSiC films with high Si/low C contents (13/10 at.%) suffered much less localized etching compared to TaNiC films. Thus, Si had a significant role in increasing the mechanical strength, corrosion resistance, and thermal stability of the TaNiSiC films.

1. Introduction

Metallic glasses are amorphous materials, free from grains, grain boundaries, and dislocations [1–3]. They have previously

* Corresponding author.
  E-mail address: maciej.kaplan@physics.uu.se (M. Kaplan).
[1] Shared first authorship.

been shown to have high corrosion and wear resistances, as well as high elastic limits [4–6], making them potential candidates for use as accident tolerant fuel cladding coatings (ATFCC) in nuclear power applications [7]. As crystalline coatings with grains and grain boundaries have been known to suffer from high corrosion rates [8], stress corrosion cracking [9], and He induced embrittlement [10], an amorphous material may therefore perform better. Light water reactors, which use borated water as a coolant at 300 °C and 7–16 MPa, often suffer from corrosion issues in the primary circuit. Borate salts are used to thermalize the neutrons coming from the fission reaction[11], but the high alkalinity of the borate salt is known to degrade the pipes due to corrosion.

The fractions and compositions of the phases constituting a crystalline alloy are governed by thermodynamics, which limits the elemental content in each of the phases[12–15]. In contrast, a metallic glass can constitute large amounts of multiple elements [16,17], enabling potent improvements in the material properties. However, the high cooling rate required to synthesize a glass restricts the size of metallic glass components. Furthermore, metallic glasses are known to crystallize at elevated temperatures as the amorphous state is metastable. These challenges have inhibited the technological applications of metallic glasses, especially at elevated temperatures. A pathway to designing metallic glasses with crystallization temperatures above 700 °C is to use refractory elements, such as W, Ta, Mo, or Nb. W- and Ta-based glasses have been observed to have the highest crystallization temperatures and mechanical strengths, but Ta has higher corrosion resistance than W [18] and Nb [19]. Ni in combination with Ta and Nb may increase the metal content of the alloy while retaining high thermal stability, mechanical properties, and corrosion resistance [19,23,24]. Mechanical strength can be increased further through addition of metalloids and/or non-metallic elements, such as B, C, and Si [20,17,21,18]. However, excess amounts of these can induce brittle behavior in the material [22].

Magnetron sputtering does not require that the elements are melted to form alloys, enabling the synthesis of coatings of refractory elements without use of high temperatures. Furthermore, the high cooling rate [25] can be utilized to synthesize metallic glasses over wide composition ranges [26], whereby composition and property relationships can be determined. In this work, combinatorial design approaches and compositional tuning [27,18,6,28–30] have been employed to enhance the material properties of TaNiSiC and TaNiC glasses, which to our knowledge have not been studied before. They are expected to form metallic glasses over wide composition ranges due to high cooling rates during sputtering and their spread in atomic radii (Ta: 147 pm, Ni: 127 pm, Si: 117 pm, and C: 77 pm) [32,33]. The naturally abundant isotopes of these elements have a low neutron scattering cross section [31], making them potential candidates as nuclear fuel cladding coatings. However, the neutron economy aspect has not been considered within this work.

The thermal, mechanical, and corrosion properties of the TaNiSiC and TaNiC alloys were investigated using annealing, X-ray diffraction, transmission electron microscopy, nanoindentation, and polarization measurements in 10 mM sodium borate. The objective of this work was to establish design rules and synergistic effects of the alloying elements by characterizing the properties of TaNiC and TaNiSiC metallic glasses.

2. Experimental

TaNiC and TaNiSiC films were deposited on three-inch Si (100) wafers using combinatorial magnetron sputtering at room temperature in a custom built ultra-high vacuum chamber, described in Ref. [34]. Targets of elemental tantalum (Ta), nickel (Ni), silicon
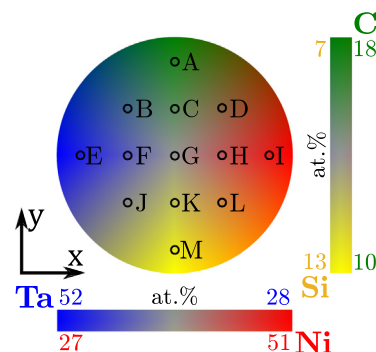

Fig. 1. Visualization of the elemental gradients on the quaternary TaNiSiC films. The position of highest concentration of each element is shown by their respective label and the highest and lowest quantity by the legends. The distance between two neighboring measurement points is 15 mm and each position is labeled A through M. The TaNiC gradient film is similar, but without the Si-rich (yellow) edge and its composition limits are stated at the beginning of the results section.

(Si), and carbon (C) with purities of at least 99.95% were used. Direct current power supplies were used for Ta, Ni, and C, while a pulsed direct current power supply was used for Si to avoid charging of the target. All depositions were carried out in argon at 0.6 Pa, and the base pressure of the system was lower than $4 \cdot 10^{-7}$ Pa. Deposition rates were determined by measuring the thickness of reference films for each sputtered material with X-ray reflectometry (XRR). Powers were subsequently chosen for each target such that the center of the wafer had a 1:1 Ta/Ni ratio. The compositional gradients within a film are illustrated in Fig. 1, and each measurement point (black circles) on every wafer is spaced 15 mm apart on a quadratic grid, with the wafer center being defined as (0, 0). The investigated materials consist of a binary TaNi, ternary TaNiC, and quaternary TaNiSiC gradient films.

The structure of the as-deposited and annealed samples was determined using X-ray diffraction (XRD) measurements in a Bruker D8 Discover with Cu Kα radiation, with line focus in Bragg–Brentano geometry, and a LynxEye XE detector. The Cu Kβ radiation was suppressed with a 0.2 mm Ni-filter, the beam spot was 5 by 5 mm^2 for each measuring point, and the detector was set to 1D mode with a 2.2° opening. Subsequent one-hour heat treatments at 400, 500, 600, and 700 °C were performed in the deposition chamber with *ex-situ* XRD measurements in between each step.

The chemical compositions along the Ta/Ni and the C/Si gradients were determined by Time-of-Flight Energy elastic recoil detection analysis (ToF-E-ERDA) at the Tandem Accelerator at Uppsala University. The measurements were carried out using 36 MeV $^{127}I^{8+}$ ions as projectile species, and the scattered ions were detected at a 45° angle with respect to the primary beam. The angle of incidence and the detection angle with respect to the sample surface of the incoming and outgoing ions was set to 22.5°. Details about the experimental system can be found in Ström et al. [35]. The POTKU software package was used for data analysis [36]. ToF-E-ERDA has a very high precision (±1 at.%) for light elements such as C with respect to quantification of relative compositional differences. An error of 5–10% of the deduced composition is expected for light elements when determining the absolute composition. A more detailed description of the uncertainties can be found in Moro et al. [37].

Cross-section and top-view transmission electron microscopy (TEM) samples have been prepared with a focused ion beam and scanning electron microscopy (FIB-SEM, FEI Strata DB235). The TEM lamellas of the $Ta_{39}Ni_{39}Si_9C_{13}$ alloy were extracted using a Ga FIB, and were subsequently attached to Cu lift-out grids. Both the cross-section and the top-view samples were thinned to electron transparency with a 30 kV Ga beam with a subsequent final

polishing step using 5 kV Ga ions in order to reduce the surface damaged volume. TEM analysis was carried out on a probe-corrected FEI Titan Themis equipped with an X-FEG and the SuperX system for energy dispersive X-ray (EDX) spectroscopy operated at 200 kV. The EDX spectral images were acquired and evaluated with the software ESPRIT (version 1.9) by Bruker. A standardless quantification method was conducted using theoretical k-factors provided by the software.

A CSM Instruments' Ultra Nano Hardness Tester equipped with a diamond Berkovich tip was used to measure the hardness and modulus of the films. The indentation depth was set to 50 nm, which is below 10% of the film thickness, to minimize substrate effects. 20 load–displacement curves were recorded for each measurement spot. The hardness (H) and the reduced elastic modulus (E_r) were determined from at least 10 load–displacement curves using the method by Oliver and Pharr [38].

Potentiodynamic polarization studies were carried out in a 10 mM sodium borate solution to determine the electrochemical stability of the films. All films had been stored in sterile and ambient conditions, and it is thus likely that a native surface oxide was present on all the films. The potential was scanned from -0.7 V to $+1.5$ V vs. Ag/AgCl (3 M NaCl) at a scan rate of 1 mV/s, the electrode area was 0.2 cm^2, and the volume of electrolyte was 4 ml. A standard three-electrode cell was used, with the films as the working electrode, a Pt counter electrode and an Ag/AgCl electrode filled with 3 M NaCl as the reference electrode. After the first polarization, the films were left overnight in the electrolyte, and a second polarization using the same parameters was conducted after 24 h. Up to three polarization measurements were conducted. The intention of these tests was to evaluate the passivity of the films in oxidizing conditions. The investigated alloys were TaNiC (position E) and TaNiSiC (positions A, E, G, I, and M), *i.e.* two compositional gradients - increasing Si content (positions A, G, and M) and increasing Ta content (positions I, G, and E).

3. Results and discussion

The investigated films had the following compositions:

(i) The binary Ta$_{65}$Ni$_{35}$ alloy,
(ii) Ternary TaNiC alloys ranging from 30–55 at.% Ta, 29–55 at.% Ni, and 14–23 at.% C,
(iii) Quaternary TaNiSiC alloys ranging from 28–52 at.% Ta, 27–51 at.% Ni, 7–13 at.% Si, and 10–18 at.% C.

The TaNiSiC gradient is illustrated in Fig. 1 together with the different measurement spots. The Ta-, Ni-, Si- and C-rich ends of the wafer are marked in blue, red, yellow and green respectively (the color coding is consistent), and an equivalent representation without Si (yellow) will be used for the TaNiC gradient. The center of the vertical and horizontal color bars represent the composition of the position G, as seen Fig. 1. The C and Si contents were constant while the Ta/Ni ratio varied along the positions E, F, G, H, and I (horizontal direction in Fig. 1). Conversely, the Ta and Ni contents were constant while the Si/C ratio varied along positions A, C, G, K, and M (vertical direction). X-ray diffraction measurements show that the TaNiC and TaNiSiC alloys were amorphous in the as-deposited state, and the reader is referred to the **Supplementary information** to see the diffractograms. The main diffraction peaks, termed 'halos', were observed between 38 and 41°. Their intensity, position, and width varied depending on the specific TaNiSiC alloy composition on the wafer, and the Si substrate reflection was visible around 69°.

TEM investigations of the Ta$_{39}$Ni$_{39}$Si$_9$C$_{13}$ alloy (center position, G, in Fig. 1) were carried out to rule out the formation of nanocrys-

tallites. The center position on the wafer was chosen since it was expected to be the best representation of all alloy compositions on the deposited gradient films. Fig. 2a shows the high angle annular dark field (HAADF) image of the film cross-section. The cross-section view depicts the presence of a columnar morphology throughout the film. Although the film appeared to have very narrow grains, the fully amorphous structure of the cross-section was further verified by selected area electron diffraction (SAED) using an aperture integrating over the full film thickness. The diffraction pattern is shown in Fig. 2b and exhibited a broad featureless ring, which was also consistent with the XRD results.

The top-view of the same sample was also investigated, and the HAADF image is shown in Fig. 2d. The film appeared to be dense and without cracks or voids. The EDX maps in Fig. 2e (cross-section) and 2f (top view) depict a chemical inhomogeneity in the film and their corresponding HAADF images in Figs. 2c and 2d. A variation in Ta and Ni was observed in the EDX maps, which gave rise to the contrast in the HAADF images, and may also have an effect on materials properties. No inhomogeneities were detectable in the EDX maps for Si and C but minor segregations may only be detected by atom probe tomography, which has a higher sensitivity for light elements [39]. A similar columnar morphology on the nanoscale was not observed previously in Ta$_{40}$Ni$_{40}$Si$_{20}$ films, which had featureless cross-sections [40]. However, the appearance of column-like morphology in amorphous films has been previously reported in other materials and is typically attributed to chemical variations [41,42], such as the TaNi variation reported herein. Idrissi et al. [43] have reported Zr-rich and Ni-rich regions in amorphous Zr$_{65}$Ni$_{35}$ thin films. Since Ni does not form carbides [14,44,45], while Ta does [45], the presence of C may therefore provide the driving force for the segregation of Ta and Ni. The limited diffusion of atoms during deposition could then lead to the formation of the column-like morphology in the film.

3.1. Effect of annealing

Crystals were observed in XRD measurements of the TaNiC alloys after one-hour annealing at 400 to 700 °C with 100 °C increments (total annealing time of four hours). The ternary Ta$_{43}$Ni$_{43}$Si$_{14}$ alloy was reported to crystallize around 700 °C [40], while Ta$_{43}$Ni$_{43}$C$_{14}$ (position M) remained amorphous after annealing at 700 °C (diffractogram in supplementary material). Higher melting points correlate with higher cohesive energies in the material and therefore increase the resistance to atomic rearrangements [46]. The melting point of carbon is twice that of Si and explains the higher thermal stability of TaNiC over TaNiSi.

Crystallites were detected in the following Ni- and C-rich alloys after annealing: Ta$_{39}$Ni$_{38}$C$_{23}$ (position A), Ta$_{34}$Ni$_{47}$C$_{19}$ (position D), Ta$_{35}$Ni$_{48}$C$_{17}$ (position H), and Ta$_{29}$Ni$_{55}$C$_{16}$ (position I) alloys (see Fig. 1 for positions). The remaining TaNiC alloys were amorphous. The crystallization of C-rich alloys was connected to the carbide formation of Ta and the phase separation between Ni and C. Ta carbides have highly negative formation enthalpies [45] leading to a strong driving force for bonding between Ta and C. The mixing enthalpies in Table 1 illustrate the binary chemical interactions between the different elements [47]. TaC interactions are more attractive compared to those of NiC and TaNi. In contrast, a phase separation is seen in the phase diagram of the NiC system between the fcc Ni and graphite [14,44].

The more energetically favorable bonds are hence between Ta and C, potentially leading to a separation of Ni. The inhomogeneous mixing of all the elements violates the empirical rules for glass formation [33]. The strong driving force for carbide formation with Ta and the phase separation of Ni and C therefore outweigh the benefit of adding C, even though high melting elements usually increase the thermal stability of metallic glasses [46]. By the same
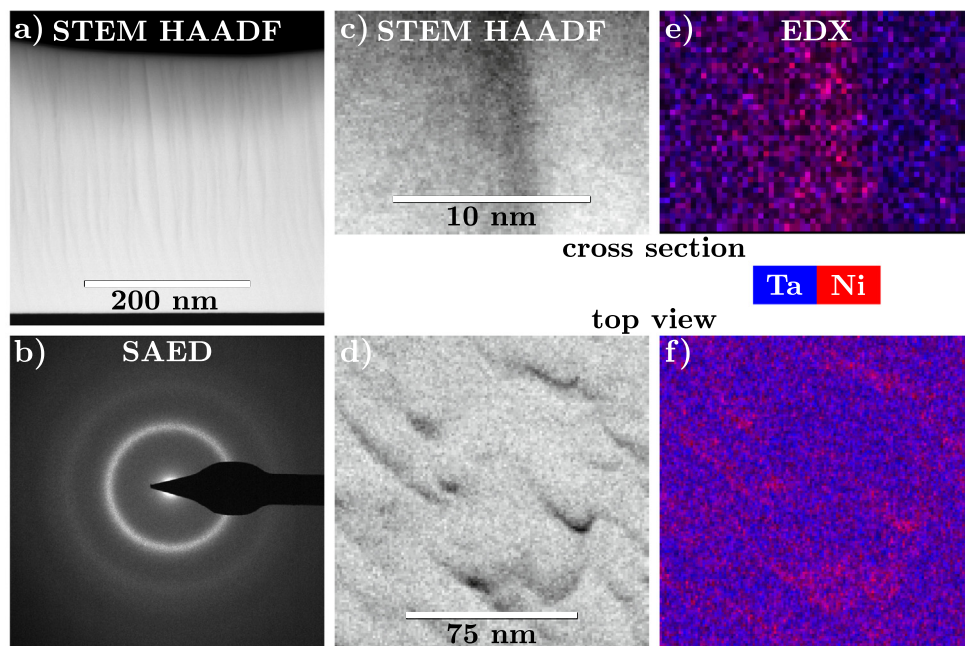
Fig. 2. TEM of images of $Ta_{39}Ni_{39}Si_9C_{13}$, STEM image and SAED of the entire film cross-section (a and b). A zoom-in on the features observed in the film cross-section (c) and top-view (d), and their EDX maps of the cross-section (e) and top-view (f).

Table 1
Mixing enthalpy, ΔH_{mix}, of binary 50–50 alloys, calculated using Miedemas semi-empirical model [47].

Binary	TaNi	TaSi	TaC	NiSi	NiC	SiC
ΔH_{mix} [kJ mol^{-1}]	−29	−56	−101	−40	−39	−39

argument, the thermal stability is expected to increase with increasing Ta content, which is also observed in the TaNiC alloys. This shows that the thermal stability of TaNiC alloys is sensitive to increasing contents of Ni and C.

Unlike the TaNiC alloys, all of the TaNiSiC alloys remained amorphous after annealing at 700 °C. The increased thermal stability of TaNiSiC over TaNiC alloys has been attributed to the addition of Si, which may have reduced the separation tendencies between fcc Ni and graphite [14]. The solubility of C in Ni is low (2 at.%) with no present intermetallic phases [44], while the solubility of Si in Ni is 15 at.% with multiple intermetallic phases [48]. The presence of intermetallic phases indicates an energetically favorable bonding between Ni and Si, which might facilitate the mixing of all components in the TaNiSiC alloy. The NiC binary subsystem is the only one which has phase separation between the terminal phases (*e.g.* fcc Ni, graphite). All the other binary combinations (TaNi, TaSi, TaC, NiSi, and SiC) have favorable bonding, as seen by the presence of compound phases in their binary phase diagrams [49,48,50,45,51]. The addition of Si may thus decrease the phase separation tendencies from a thermodynamic point of view compared to the TaNiC system. The high melting point of C as well as its small radius may account for the higher thermal stability of the TaNiSiC alloys over previously studied TaNiSi thin films [40]. These results indicate that combination of Si and C produce a glass with superior thermal stability compared to a material containing just one of these elements.

Structural changes were observed in the TaNiSiC films despite the absence of crystallites. The diffraction halos of all alloys were fitted with a pseudo-Voigt profile after each annealing step at 400 to 700 °C. The position of the halo was extracted, as shown in the inset top right in Fig. 3b, for the $Ta_{39}Ni_{39}Si_9C_{13}$ alloy (position G). The positions of the halos of the as-deposited alloys are shown by the datapoints at 25 °C, for changing Ta/Ni ratios (Fig. 3a) and for changing Si/C ratios (Fig. 3b). It can be seen that the halo positions shifted to higher angles for increasing Ni and Si contents.

After annealing from 400 to 700 °C, the halos moved to higher angles for all TaNiSiC alloys, as can be seen in Fig. 3. The systematic shifts toward higher angles of all the TaNiSiC films correspond to shorter inter-atomic distances. Each line is a linear fit to the datapoints for one alloy and represents the position change of the halo induced by the annealing. The slope of each line varied with composition and was steepest for the Ni-rich alloy ($Ta_{28}Ni_{52}Si_8C_{12}$). Changing the Si/C ratio did not significantly affect the slope, as seen in Fig. 3b. The changes in halo positions/interatomic distances seem to have had an impact on the mechanical properties of the alloys.

3.2. Mechanical properties of the ternary TaNiC alloys

The hardnesses of the TaNiC alloys as a function of composition are shown in Fig. 4. The blue (Ta), red (Ni), and green (C) lines represent the content of each element across the film, and the black circles show the corresponding hardness for the position on the film. The inset in the top left shows the direction of progression along the film. The Ni-rich alloy exhibited a hardness of 7.0 GPa, which was lower than any other deposited alloy and deviates from the trend of the other alloys in Fig. 4a. SEM micrographs revealed micro-meter sized cracks on the Ni-rich side (position I) of the gradient film (data not shown). The measurements of the mechanical properties were therefore deemed unreliable and excluded from further analysis for this composition (position I, $Ta_{29}Ni_{55}C_{16}$). The hardness increased from 8.4 ± 0.5 to 10.2 ± 0.8 GPa with increasing Ta content from 36 to 55 at.% (Fig. 4a). How-
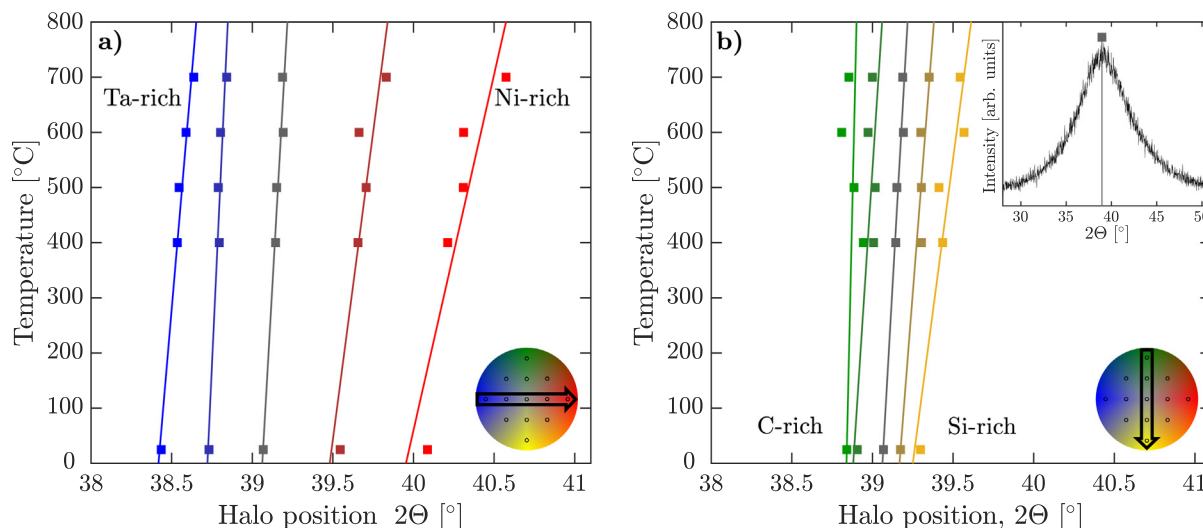
Fig. 3. The position of the diffraction halos in XRD measurements along the Ta/Ni (a) and Si/C (b) gradients of the TaNiSiC film. Each trend line represents one composition indicating the change of the halo position with each annealing cycle.
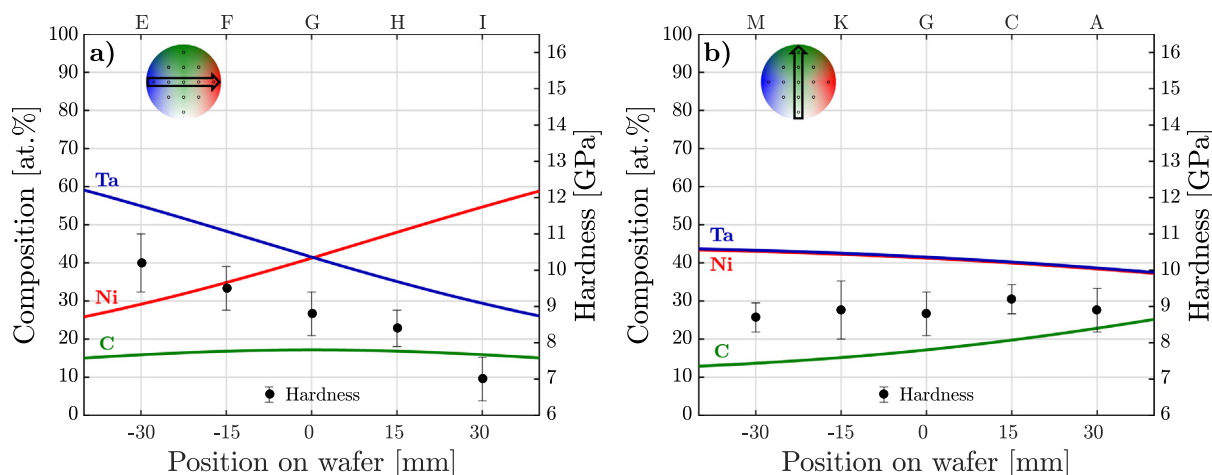

Fig. 4. The hardness and composition as a function of position along the Ta/Ni (a) and Si/C (b) gradients for the TaNiC alloys, where the hardness and standard deviation is denoted by the black markers and error bars on the right y-axis, while the composition of each element by the colored lines on the left y-axis.

ever, the hardnesses of the TaNiC alloys were constant within the standard deviation when varying the C content between 14 and 23 at.%, as seen in Fig. 4b. The binary $Ta_{65}Ni_{35}$ alloy had a hardness of 10.1 ± 0.6 GPa and a reduced modulus of 152 ± 6 GPa, similar to the mechanical properties of $Ta_{38}Ni_{62}$ bulk metallic glass which had a hardness of 9.6 GPa and an elastic modulus of 175 GPa [23]. The binary alloy had a Ta/Ni ratio of almost 2:1, and was similar for the ternary $Ta_{55}Ni_{29}C_{16}$ (position E) alloy, which had a hardness and modulus of 10.2 ± 0.8 GPa and 170 ± 8 GPa, respectively.

The Ta/Ni ratio was the main parameter to tune when designing TaNiC glasses with high hardness and modulus, whereas the addition of C to TaNi alloys did not change the mechanical properties within the studied concentration range. Furthermore, the hardness of the Ta-rich (position E) composition increased from 10.2 GPa to 12.9 GPa as a consequence of annealing to 700 °C. Similar changes and trends were observed for the TaNiSiC alloys and will be discussed in the following section.

3.3. Mechanical properties of the quaternary TaNiSiC alloys

The highest observed hardness among the as-deposited TaNi, TaNiC, and TaNiSiC alloys was 12.4 ± 0.4 GPa (position E: $Ta_{52}Ni_{28}$-

Si_8C_{12}), while the lowest was 8.4 ± 0.5 GPa (position H: $Ta_{35}Ni_{48}$-C_{17}). The hardnesses along both gradients of the as-deposited and annealed TaNiSiC alloys (circles and triangles respectively) are shown in Fig. 5. The hardnesses of the as-deposited alloys along the Ta/Ni gradient increased from 8.9 ± 0.4 GPa to 12.4 ± 0.4 GPa with increases in Ta content from 28 to 52 at.%. This is similar to the TaNiC alloys, where the hardness increased along the Ta/Ni gradient. Increasing the C content from 10 to 18 at.% (i.e. decreasing the Si content from 13 to 7 at.%) in the TaNiSiC film shows that the hardness increased from 9.6 ± 0.3 GPa to 10.9 ± 0.5 GPa. The increase along both the Ta/Ni and Si/C gradients are approximately the same per at.%, in contrast to the TaNiC alloys which do not show changes in hardness for C contents between 14–23 at.%. The presence of Si has a significant role in increasing the hardness in quaternary TaNiSiC alloys, and the combined effect of Si and C is seen to have a synergistic effect on the mechanical properties compared to C alone.

The results show that the hardness and modulus of the TaNiSiC alloys are higher compared to the TaNiC alloys, and a further increase in C content could further increase the hardness and modulus. The changes in hardness per atomic percent are of similar magnitudes along both the Ta/Ni and Si/C gradients. However,
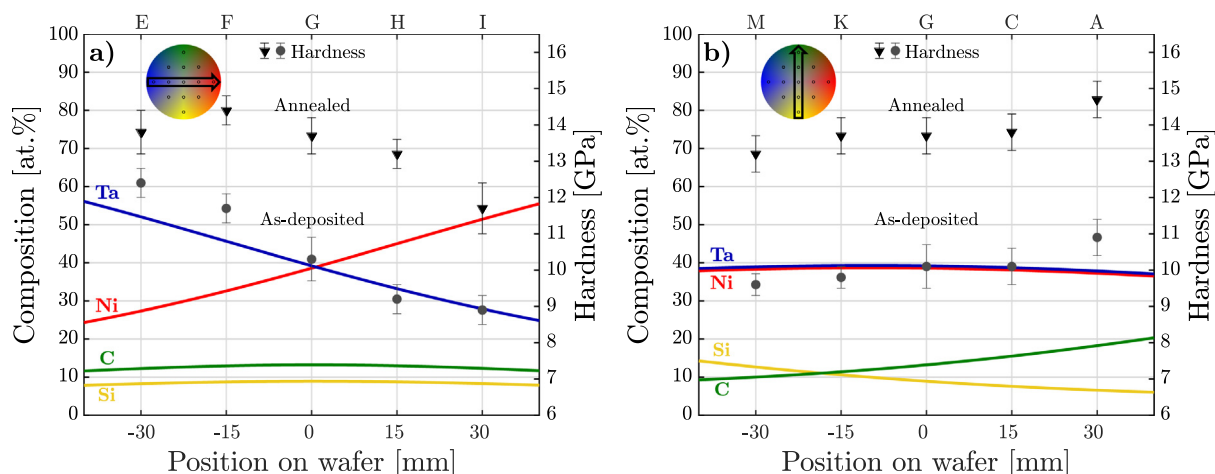
Fig. 5. The hardness and composition as a function of position along the Ta/Ni (a) and Si/C (b) gradients of the TaNiSiC alloys. The colored lines represent the composition on the left y-axis of each element by each colored line, and the hardness on the right y-axis of as-deposited (circles) and annealed (triangles) and standard deviation (error bars) of the TaNiSiC alloys.

the changes in mechanical properties with increasing C content are less pronounced compared to additions of C in crystalline refractory metals, where 5 at.% C increases the hardness by at least 4 GPa [52–54].

The hardnesses of the TaNiSiC alloys after annealing at 700 °C are shown in Fig. 5 as the triangular markers. As mentioned previously, all alloys remained amorphous during the annealing, but the average atomic distance was seen to decrease over the course of annealing. The hardnesses of the TaNiSiC alloys increased between 1.4 and 4.0 GPa upon annealing (see supplementary material for details). The increase in hardness was related to the decrease of average atomic distance in the TaNiSiC alloys, which was shown in Fig. 3. The decrease in average atomic distance can be associated with a decrease in free volume which may explain the increased mechanical strength [55,56]. It is therefore concluded that the hardness and modulus increases due to structural effects as a consequence of the annealing.

The hardness increase along the Si/C gradient was close to 36%, irrespective of the ratio of Si and C, as seen in Fig. 5. However, along the Ta/Ni gradient, the hardness increase was largest on the Ni-side (position H in Fig. 5a) by up to 43% and lowest on the Ta-rich side, where it is 11% (position E). As was seen in the diffraction measurements, the largest changes in average atomic distance was for the alloys containing the most Ni. These findings indicate that the diffusion of Ni has an earlier onset as compared to Ta, whereas differences in the diffusion of Si and C atoms are not clear from the present data. Nonetheless, annealing is a useful tool for increasing the mechanical strength in the TaNiSiC system, to tune the mechanical properties of the alloys.

3.4. Effect of corrosion on the TaNiSiC alloys

Potentiodynamic polarization measurements were conducted every 24 h on three consecutive days and the films were left immersed in the electrolyte overnight. A detailed description can be found in the Experimental section. All values of potentials are stated vs. Ag/AgCl (3 M NaCl) unless mentioned otherwise.

3.4.1. Effect of Ta/Ni content on corrosion resistance

The potentiodynamic polarization curves of TaNiSiC films containing 28 and 52 at.% Ta on Day 1 are shown in Fig. 6a. The film with 52 at.% Ta had lower current densities than the film with 28 at.% Ta at potentials between −0.2 V and +1.5 V vs. Ag/AgCl (3 M NaCl). The lower current densities imply a higher corrosion

resistance due the formation of a higher content of Ta oxides on the surface, which is in agreement with several studies of Ta alloys [57–61]. Pourbaix diagrams of Ta [62] show that Ta_2O_5 is stable at all the herein applied potentials [63] and pH conditions. The increased corrosion resistance is therefore likely due to the proportional increase of Ta oxides on the surface.

Both of the TaNiSiC films with high and low Ta contents showed an increase in current densities at potentials above 1.0 V. According to several studies, this may be attributed to an increased oxidation of Ni [64–66]. In these previous studies of Ni alloys, a steep increase (3–5 orders of magnitude) in the oxidation current at potentials above 0.5 V was observed, whereas the studied TaNiSiC films show smaller increases (2 orders of magnitude) in oxidation above 1.0 V. This indicates that the Ta oxides may have contributed to slowing the oxidation of the film as increasing the Ta content appeared to reduce the current densities by one order of magnitude at the most oxidizing potentials, as seen in Fig. 6a.

There may also be an added kinetic stabilization from the sputtering process used to synthesize the films [67–69]. The high cooling rates may have limited the diffusion of Ta and Ni atoms. This relatively homogeneous distribution of Ta and Ni atoms is expected to reduce the selective dissolution of Ni, demonstrating the utility of sputtered metallic glass coatings.

The potentiodynamic polarization data of $Ta_{39}Ni_{39}Si_9C_{13}$ film on Day 1 and Day 2 is shown in Fig. 6b. Significantly lower current densities were recorded on Day 2 compared to Day 1, indicating increased interfacial passivity, and has been attributed to the increase in Ni oxidation occurring after 1 V from Day 1, which then contributed to the lower currents observed on Day 2. The Pourbaix diagram for Ni shows that Ni alloys are expected to form a surface oxide rich in $Ni(OH)_2$ at ∼−0.2 V, Ni_3O_4 at ∼0.6 V, Ni_2O_3 at ∼1.0 V and NiO_2 above ∼1.1 V. Ultimately, as Ni is the least noble of all the elements, it is both the increased oxidation and the very low solubility of the Ni oxides in the alkaline environment that determines the corrosion resistance of the TaNiSiC films [70,71].

The data thus shows that the alloying of Ta and Ni resulted in a highly stable corrosion resistant surface oxide up to 1.0 V. TaNiSiC films with higher Ta contents produced proportionally higher concentrations of Ta oxides on the surface, reducing the current densities at all the measured potentials. Immersion of the TaNiSiC films for longer periods of time could lead to a slow dissolution of Ni, and an enrichment of Ta on the surface.

A table summarizing all the corrosion potentials and corrosion current densities is provided in the supplementary information.
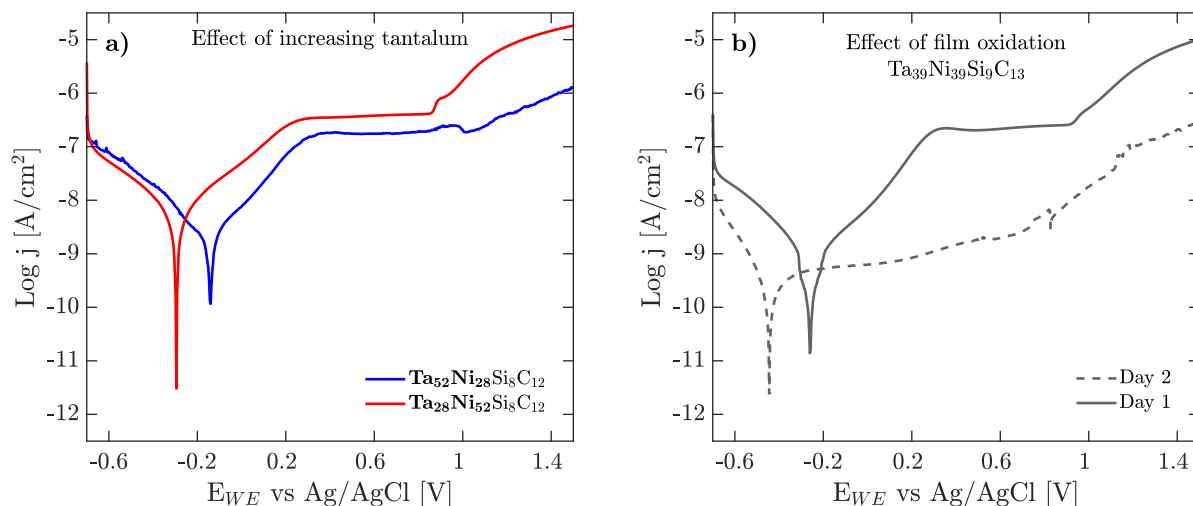
Fig. 6. (a) Potentiodynamic polarization curves of TaNiSiC films with different Ta content. The potential range was –0.7 to 1.5 V vs. Ag/AgCl (3 M NaCl). (b) Effect of film oxidation. Day 1 is shown using solid lines and Day 2 is shown using a dashed line. Note than an increase in Ta leads to a decrease in Ni.

On Day 1, the corrosion potentials (E_{corr}) fall between -0.29 to -0.14 V and the corrosion current densities (j_{corr}) are in the order of 10^{-7} to 10^{-8} A/cm^2. The passive regions spanned between 0.38 to 1.0 V. As mentioned previously, on Day 2, the corrosion current densities were an order of magnitude lower than on Day 1, indicating an increased passivity. The corrosion potential was also lower on Day 2 compared to Day 1, indicating lower contributions of current from cathodic reactions.

3.4.2. Effect of Si/C content on corrosion resistance

The above mentioned potentiodynamic polarization procedure in 10 mM sodium borate was also conducted on the films with varying Si/C content (from 7 to 13 at.% for Si and 18 to 10 at.% for C), at positions A, G, M, from − 0.7 to + 1.5 V. The recorded cur-rent densities in these films overlapped and a trend with respect to the changes in Si or C composition could not be obtained. The potentiodynamic polarization data has thus been relegated to the supplementary information. Changing the Si content from 7 to 13 at.% (and thus reducing the C content from 18 to 10 at.%) may not have elicited significant differences in the current densities as both Si and C are group 4 elements, neither of which are expected to undergo corrosion in the tested conditions [62]. Even if the Si content was increased (and the C content reduced), the total p-element concentration was still unchanged, potentially accounting for the similar electrochemical responses. The data extracted from Tafel extrapolations such as the corrosion current densities and corrosion potential have nonetheless been provided in the supplementary information and show similar values for all the films.
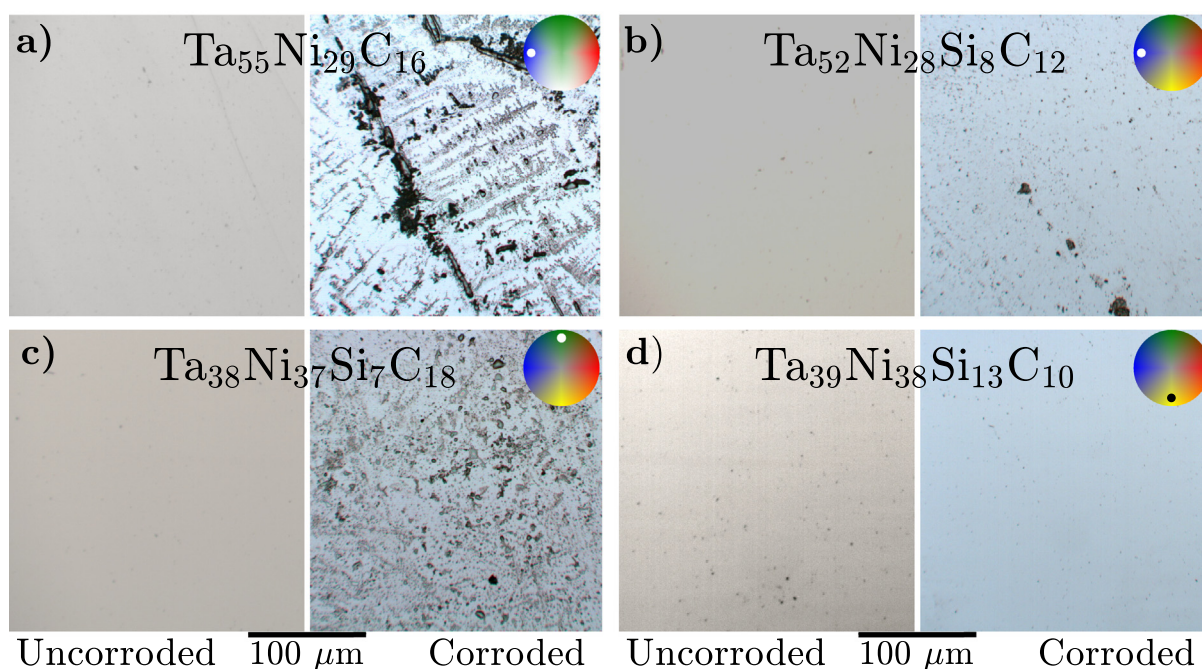

Fig. 7. Optical images of TaNiC and TaNiSiC films before and after three potentiodynamic polarization measurements. The inset in the top right shows the measured position on the film. The films were kept immersed in the solution between the polarizations.

Table 2
Hardness before and after annealing or corrosion measurements.

Composition [at.%]	H [GPa]	H^{corr} [GPa]	$H^{700\ °C}$ [GPa]
$Ta_{38}Ni_{37}Si_7C_{18}$	10.9 ± 0.5	10.5 ± 0.7	14.7 ± 0.5
$Ta_{52}Ni_{28}Si_8C_{12}$	12.4 ± 0.4	12.8 ± 1	13.8 ± 0.6
$Ta_{39}Ni_{38}Si_{13}C_{10}$	9.6 ± 0.3	10.6 ± 0.6	13.2 ± 0.6

Literature studies show that SiO_2 is stable under the imposed conditions since it has very low solubility and is resistant to further oxidation [72,73]. Pourbaix diagrams of Si also show that SiO_2 is electrochemically stable to oxidation at this range of pH and potential [62]. Of all the tested films, only the Si-free TaNiC film showed a very noisy response on Day 3, as much of the film was lost during the test (shown in Fig. 5 of the supplementary information). For the rest of the films, the polarizations on Day 3 overlapped with those on Day 2, especially in the anodic portions of the curves making it difficult to identify any trend with respect to Si/C composition.

Despite the absence of significant differences in the potentiodynamic polarization measurements, optical microscopy revealed large differences in the etching of the films. Fig. 7 shows the surfaces of the TaNiSiC alloys with different compositions before and after the potentiodynamic polarization measurements in 10 mM sodium borate. Figs. 7a and 7b show a large difference in the surface conditions on the films between a TaNiC and TaNiSiC film with 8 at.% Si. The TaNiC film appears to have undergone severe etching with some parts of the film being lost entirely. Subsequent hardness measurements were impossible due to the destroyed surface. In contrast, the TaNiSiC films shown in Fig. 7 appear intact, and subsequent measurements of their hardness and modulus were unchanged after the corrosion and are shown in Table 2. This indicates that the corrosion of the TaNiSiC films did not deteriorate their mechanical integrity. The TaNiSiC film with the highest Si content, as seen in Fig. 7d, appears least etched (or is perhaps more homogeneously etched) after corrosion compared to all the other films. The corrosion resistance seems to increase significantly with increasing Si contents, with higher Si contents appearing to protect the film from localized etching more efficiently than that of Ta, which is very important for developing lighter and less expensive alloys.

4. Summary and conclusions

Further testing under high pressure, temperature, and neutron flux is necessary to determine the suitability of TaNiSiC films as accident tolerant fuel cladding coatings. However, all TaNiSiC films had an increased thermal stability, hardness, modulus, and corrosion resistance compared to the TaNiSi [17] and TaNiC ternaries. This may be due to a synergistic effect between Si and C. An additional increase in hardness was obtained after annealing of the TaNiSiC and TaNiC alloys, which was traced back to shorter inter-atomic distances within the material.

The separation of Ni and C may be larger in the TaNiC alloys compared to the TaNiSiC alloys due to the absence of Si. The TaNiC alloys may have been more susceptible to preferential etching of Ni, which highlights the importance of homogeneous mixing of the constituents in a metallic glass. The design of a corrosion resistant and hard TaNiSiC coatings was obtained by the addition of elements which have thermodynamically favorable mixing, such as TaC and/or NiSi. Phase separation between the pure components, such as in the NiC system [44], could thus be avoided. Hence, even small contents of an element (in this case Si) had a large impact on the properties of the TaNiSiC films by mediating the separation tendencies, as reflected in the hardness and corrosion resistance. Homogeneous mixing of the elements is therefore not only impor-

tant for glass formation [33] and thermal stability, but also for the material properties of a metallic glass.

Author contribution

Maciej Kaplan: Conceptualization, software, investigation, formal analysis, original draft, review & editing. **Aishwarya Srinath:** Investigation, formal analysis, original draft, review & editing. **Lars Riekehr:** Investigation, review & editing. **Leif Nyholm:** Supervision, review & editing, funding acquisition. **Björgvin Hjörvarsson:** Supervision, review & editing, funding acquisition. **Stefan Fritze:** Conceptualization, investigation, formal analysis, review & editing.

Data Availability

The raw/processed data required to reproduce these findings cannot be shared at this time due to technical or time limitations.

Declaration of Competing Interest

The authors declare that they have no known competing financial interests or personal relationships that could have appeared to influence the work reported in this paper.

Appendix A. Supplementary material

Supplementary data associated with this article can be found, in the online version, at https://doi.org/10.1016/j.matdes.2022.110827.

References

[1] W. Buckel, R. Hilsch, Supraleitung und Widerstand von Zinn mit Gitterstörungen, Zeitschrift für Physik 131 (1952) 420–442, https://doi.org/10.1007/BF01329552.

[2] W. Klement, R.H. Willens, P. Duwez, Non-crystalline Structure in Solidified Gold-Silicon Alloys, Nature 187 (1960) 869–870, https://doi.org/10.1038/187869b0.

[3] Y. Yang, J. Zhou, F. Zhu, Y. Yuan, D.J. Chang, D.S. Kim, M. Pham, A. Rana, X. Tian, Y. Yao, S.J. Osher, A.K. Schmid, L. Hu, P. Ercius, J. Miao, Determining the three-dimensional atomic structure of an amorphous solid, Nature 592 (2021) 60–64, https://doi.org/10.1038/s41586-021-03354-0.

[4] M. Ishida, H. Takeda, N. Nishiyama, K. Kita, Y. Shimizu, Y. Saotome, A. Inoue, Wear resistivity of super-precision microgear made of Ni-based metallic glass, Mater. Sci. Eng.: A 449–451 (Mar. 2007) 149–154, https://doi.org/10.1016/j.msea.2006.02.300.

[5] Q.K. Jiang, P. Liu, Y. Ma, Q.P. Cao, X.D. Wang, D.X. Zhang, X.D. Han, Z. Zhang, J.Z. Jiang, Super elastic strain limit in metallic glass films, Scientific Reports 2 (Dec. 2012) 852, https://doi.org/10.1038/srep00852.

[6] M.-X. Li, S.-F. Zhao, Z. Lu, A. Hirata, P. Wen, H.-Y. Bai, M. Chen, J. Schroers, Y. Liu, W.-H. Wang, High-temperature bulk metallic glasses developed by combinatorial methods, Nature 569 (May 2019) 99–103, https://doi.org/10.1038/s41586-019-1145-z.

[7] C. Tang, M. Stueber, H.J. Seifert, M. Steinbrueck, Protective coatings on zirconium-based alloys as accident-tolerant fuel (ATF) claddings, Corros. Rev. 35 (Aug. 2017) 141–165, https://doi.org/10.1515/corrrev-2017-0010.

[8] K.A. Terrani, Accident tolerant fuel cladding development: Promise, status, and challenges, J. Nucl. Mater. 501 (Apr. 2018) 13–30, https://doi.org/10.1016/j.jnucmat.2017.12.043.

[9] P.L. Andresen, Stress Corrosion Cracking of Current Structural Materials in Commercial Nuclear Power Plants, Corrosion 69 (Oct. 2013) 1024–1038, https://doi.org/10.5006/0801.

[10] S.-H. Li, J.-T. Li, W.-Z. Han, Radiation-Induced Helium Bubbles in Metals, Materials 12 (Mar. 2019) 1036, https://doi.org/10.3390/ma12071036.

[11] D. Van Rooyen, H. Copson, W. Berry, Corrosion behavior of nickel-chromium-iron alloy 600 in borated pressurized water reactor environments, Corrosion 25 (5) (1969) 194–198, https://doi.org/10.5006/0010-9312-25.5.194.

[12] A. Cottrell, An Introduction to Metallurgy. Edward Arnold Publishing Limited, 2nd ed., 1971.

[13] W.L. Johnson, Thermodynamic and kinetic aspects of the crystal to glass transformation in metallic materials, Prog. Mater. Sci. 30 (2) (1986) 81–134, https://doi.org/10.1016/0079-6425(86)90005-8.

[14] A. Gabriel, C. Chatillon, and I. Ansara, "Thermochemical and phase diagram analysis of the Ni-C, Co-C, and Co-Ni-C systems," High temperature science, 1988.

[15] B. Cantor, I. Chang, P. Knight, A. Vincent, Microstructural development in equiatomic multicomponent alloys, Materials Science and Engineering: A 375–377 (July 2004) 213–218, https://doi.org/10.1016/j.msea.2003.10.257.

[16] M. Lucaci, D. Patroi, V. Tsakiris, M.V. Lungu, E. Manta, A. Iorga, Studies on Fe-Cr-Ni-Si-B Bulk Metallic Glass for Automotive Applications, Advanced Materials Research 1114 (July 2015) 68–75, https://doi.org/10.4028/www.scientific.net/AMR.1114.68.

[17] J.M. McGlone, K.R. Olsen, W.F. Stickle, J.E. Abbott, R.A. Pugliese, G.S. Long, D.A. Keszler, J.F. Wager, TaWSi amorphous metal thin films: composition tuning to improve thermal stability, MRS Communications 7 (Sept. 2017) 715–720, https://doi.org/10.1557/mrc.2017.77.

[18] T. Tryggvason, A. Tryggvason, S. Karlsdottir, A. Ingason, U. Arnalds, F. Magnus, Corrosion resistance of W and Ta based amorphous coatings in a geothermal steam environment – A combinatorial study, Geothermics 88 (Nov. 2020) 101859, https://doi.org/10.1016/j.geothermics.2020.101859.

[19] A. Kawashima, H. Habazaki, K. Hashimoto, Highly corrosion-resistant Ni-based bulk amorphous alloys, Materials Science and Engineering: A 304–306 (May 2001) 753–757, https://doi.org/10.1016/S0921-5093(00)01587-2.

[20] J. Kim, J.S. Kyeong, M.-H. Ham, A.M. Minor, D.H. Kim, E.S. Park, Development of Mo-Ni-Si-B metallic glass with high thermal stability and H versus E ratios, Materials & Design 98 (May 2016) 31–40, https://doi.org/10.1016/j.matdes.2016.02.090.

[21] J.T. Kim, S.H. Hong, X. Bian, P.K. Gokuldoss, K. Song, J. Eckert, J.M. Park, K.B. Kim, Effect of boron addition on thermal and mechanical properties of Co-Cr-Mo-C-(B) glass-forming alloys, Intermetallics 99 (Aug. 2018) 1–7, https://doi.org/10.1016/j.intermet.2018.05.006.

[22] W.L. Johnson, A.R. Williams, Structure and properties of transition-metal-metalloid glasses based on refractory metals, Physical Review B 20 (Aug. 1979) 1640–1655, https://doi.org/10.1103/PhysRevB.20.1640.

[23] Y. Wang, Q. Wang, J. Zhao, C. Dong, Ni–Ta binary bulk metallic glasses, Scripta Mater. 63 (2) (2010) 178–180, https://doi.org/10.1016/j.scriptamat.2010.03.044.

[24] W. Yao, Q. Cao, S. Liu, X. Wang, H. Fecht, A. Caron, D. Zhang, J. Jiang, Tailoring nanostructured Ni-Nb metallic glassy thin films by substrate temperature, Acta Mater. (May 2020) 13–26, https://doi.org/10.1016/j.actamat.2020.04.046.

[25] T.W. Barbee, W.H. Holmes, D.L. Keith, M.K. Pyzyna, G. Ilonca, Synthesis of amorphous niobium-nickel alloys by vapor quenching, Thin Solid Films 45 (Sept. 1977) 591–599, https://doi.org/10.1016/0040-6090(77)90251-6.

[26] M.-X. Li, Y.-T. Sun, C. Wang, L.-W. Hu, S. Sohn, J. Schroers, W.-H. Wang, Y.-H. Liu, Data-driven discovery of a universal indicator for metallic glass forming ability, Nat. Mater. 21 (Feb. 2022) 165–172, https://doi.org/10.1038/s41563-021-01129-6.

[27] M.M. Khan, I. Shabib, W. Haider, A combinatorially developed Zr-Ti-Fe-Al metallic glass with outstanding corrosion resistance for implantable medical devices, Scripta Mater. 162 (Mar. 2019) 223–229, https://doi.org/10.1016/j.scriptamat.2018.11.011.

[28] M. Kaplan, G.K. Pálsson, D.M. Holzapfel, J.M. Schneider, B. Hjörvarsson, Phase formation and thermal stability of amorphous zrnbcrmo thin films, Journal of Non-Crystalline Solids: X 9–10 (2021) 100061, https://doi.org/10.1016/j.nocx.2021.100061.

[29] N. Liu, T. Ma, C. Liao, G. Liu, R.M.O. Mota, J. Liu, S. Sohn, S. Kube, S. Zhao, J.P. Singer, J. Schroers, Combinatorial measurement of critical cooling rates in aluminum-base metallic glass forming alloys, Scientific Reports 11 (Dec. 2021) 3903, https://doi.org/10.1038/s41598-021-83384-w.

[30] B. Putz, O. Milkovic, G. Mohanty, R. Ipach, L. Pethö, J. Milkovicová, X. Maeder, T. Edwards, P. Schweizer, M. Coduri, K. Saksl, and J. Michler, "Structural characterisation of Cu-Zr thin film combinatorial libraries with Synchrotron radiation at the limit of crystallinity," Materials & Design, p. 110675, Apr. 2022. doi:10.1016/j.matdes.2022.110675.

[31] V.F. Sears, Neutron scattering lengths and cross sections, Neutron News 3 (Aug. 2006) 26–37, https://doi.org/10.1080/10448639208218770.

[32] C. Kittel, Introduction to Solid State Physics. Wiley, 8th ed., 2004.

[33] A. Inoue, Stabilization of metallic supercooled liquid and bulk amorphous alloys, Acta Mater. 48 (Jan. 2000) 279–306, https://doi.org/10.1016/S1359-6454(99)00300-6.

[34] A. Frisk, The Importance of Controlling Composition to Tailor the Properties of Magnetic Thin Films. PhD dissertation, Uppsala University, Uppsala, Nov. 2016.

[35] P. Ström, P. Petersson, M. Rubel, G. Possnert, A combined segmented anode gas ionization chamber and time-of-flight detector for heavy ion elastic recoil detection analysis, Rev. Sci. Instrum. 87 (10) (2016) 103303, https://doi.org/10.1063/1.4963709.

[36] K. Arstila, J. Julin, M. Laitinen, J. Aalto, T. Konu, S. Kärkkäinen, S. Rahkonen, M. Raunio, J. Itkonen, J.-P. Santanen, T. Tuovinen, T. Sajavaara, Potku – new analysis software for heavy ion elastic recoil detection analysis, Nucl. Instrum. Methods Phys. Res., Sect. B 331 (2014) 34–41, https://doi.org/10.1016/j.nimb.2014.02.016.

[37] M. Moro, R. Holenák, L. Zendejas Medina, U. Jansson, D. Primetzhofer, Accurate high-resolution depth profiling of magnetron sputtered transition metal alloy films containing light species: A multi-method approach, Thin Solid Films 686 (2019) 137416, https://doi.org/10.1016/j.tsf.2019.137416.

[38] W. Oliver, G. Pharr, An improved technique for determining hardness and elastic modulus using load and displacement sensing indentation experiments, J. Mater. Res. 7 (June 1992) 1564–1583, https://doi.org/10.1557/JMR.1992.1564.

[39] D. Shinde, S. Fritze, M. Thuvander, P. Malinovskis, L. Riekehr, U. Jansson, K. Stiller, Elemental distribution in CrNbTaTiW-C high entropy alloy thin films, Microsc. Microanal. 25 (2) (2019) 489–500, https://doi.org/10.1017/S1431927618016264.

[40] J.M. McGlone, K.R. Olsen, W.F. Stickle, J.E. Abbott, R.A. Pugliese, G.S. Long, D.A. Keszler, J.F. Wager, Ta-based amorphous metal thin films, J. Alloy. Compd. 650 (Nov. 2015) 102–105, https://doi.org/10.1016/j.jallcom.2015.07.226.

[41] P. Kontis, M. Köhler, S. Evertz, Y.-T. Chen, V. Schnabel, R. Soler, J. Bednarick, C. Kirchlechner, G. Dehm, D. Raabe, J. Schneider, B. Gault, Nano-laminated thin film metallic glass design for outstanding mechanical properties, Scripta Mater. 155 (Oct. 2018) 73–77, https://doi.org/10.1016/j.scriptamat.2018.06.015.

[42] P. Malinovskis, S. Fritze, J. Palisaitis, E. Lewin, J. Patscheider, P.O.A. Persson, and U. Jansson, "Synthesis and characterisation of nanocomposite mo-fe-b thin films deposited by magnetron sputtering," Materials, vol. 14, no. 7, 2021. doi:10.3390/ma14071739.

[43] H. Idrissi, M. Ghidelli, A. Béché, S. Turner, S. Gravier, J.J. Blandin, J.P. Raskin, D. Schryvers, T. Pardoen, Atomic-scale viscoplasticity mechanisms revealed in high ductility metallic glass films, Scientific Reports 9 (2019) 1–11, https://doi.org/10.1038/s41598-019-49910-7.

[44] J. Jeon, S.-Y. Kwon, D. Lindberg, M.-K. Paek, Thermodynamic Modeling of Ni-C, Co-C, and Ni-Co-C Liquid Alloys Using the Modified Quasichemical Model, Metallurgical and Materials Transactions B 52 (Feb. 2021) 59–68, https://doi.org/10.1007/s11663-020-01995-6.

[45] K. Frisk and A. Fernández Guillermet, "Gibbs energy coupling of the phase diagram and thermochemistry in the tantalum-carbon system," Journal of Alloys and Compounds, vol. 238, pp. 167–179, May 1996. doi:10.1016/0925-8388(96)02197-4.

[46] C. Cao, D. Ding, D. Zhao, E. Axinte, H. Bai, W. Wang, Correlation between glass transition temperature and melting temperature in metallic glasses, Materials & Design 60 (Aug. 2014) 576–579, https://doi.org/10.1016/j.matdes.2014.04.021.

[47] A. Takeuchi, A. Inoue, Classification of Bulk Metallic Glasses by Atomic Size Difference, Heat of Mixing and Period of Constituent Elements and Its Application to Characterization of the Main Alloying Element, Mater. Trans. 46 (12) (2005) 2817–2829, https://doi.org/10.2320/matertrans.46.2817.

[48] T. Tokunaga, K. Nishio, H. Ohtani, M. Hasebe, Thermodynamic assessment of the Ni–Si system by incorporating ab initio energetic calculations into the CALPHAD approach, Calphad 27 (June 2003) 161–168, https://doi.org/10.1016/S0364-5916(03)00049-X.

[49] Z. Guo, W. Yuan, Y. Sun, Z. Cai, Z. Qiao, Thermodynamic Assessment of the Si-Ta and Si-W Systems, Journal of Phase Equilibria and Diffusion 30 (Oct. 2009) 564–570, https://doi.org/10.1007/s11669-009-9579-x.

[50] J. Gröbner, H.L. Lukas, F. Aldinger, Thermodynamic calculation of the ternary system Al-Si-C, Calphad 20 (June 1996) 247–254, https://doi.org/10.1016/S0364-5916(96)00027-2.

[51] I. Ansara, M. Selleby, Thermodynamic analysis of the Ni–Ta system, Calphad 18 (Jan. 1994) 99–107, https://doi.org/10.1016/0364-5916(94)90011-6.

[52] S. Fritze, M. Hans, L. Riekehr, B. Osinger, E. Lewin, J. Schneider, U. Jansson, Influence of carbon on microstructure and mechanical properties of magnetron sputtered TaW coatings, Materials & Design 196 (Nov. 2020) 109070, https://doi.org/10.1016/j.matdes.2020.109070.

[53] S. Fritze, P. Malinovskis, L. Riekehr, L. von Fieandt, E. Lewin, U. Jansson, Hard and crack resistant carbon supersaturated refractory nanostructured multicomponent coatings, Scientific Reports 8 (2018) 14508, https://doi.org/10.1038/s41598-018-32932-y.

[54] S. Fritze, M. Chen, L. Riekehr, B. Osinger, M. Sortica, A. Srinath, A. Menon, E. Lewin, D. Primetzhofer, J. Wheeler, and U. Jansson, "Magnetron sputtering of carbon supersaturated tungsten films – a chemical approach to increase strength," Materials & Design, vol. 208, p. 109874, 10 2021. doi:10.1016/j.matdes.2021.109874.

[55] F. Spaepen, A microscopic mechanism for steady state inhomogeneous flow in metallic glasses, Acta Metall. 25 (Apr. 1977) 407–415, https://doi.org/10.1016/0001-6160(77)90232-2.

[56] T. Egami, Formation and deformation of metallic glasses: Atomistic theory, Intermetallics 14 (Aug. 2006) 882–887, https://doi.org/10.1016/j.intermet.2006.01.004.

[57] A. El-Moneim, E. Akiyama, H. Habazaki, A. Kawashima, K. Asami, K. Hashimoto, The corrosion behaviour of sputter-deposited amorphous Mn-Ta alloys in 0.5 M NaCl solution, Corros. Sci. 39 (Oct. 1997) 1965–1979, https://doi.org/10.1016/S0010-938X(97)00089-9.

[58] A. El-Moneim, E. Akiyama, H. Habazaki, A. Kawashima, K. Asami, K. Hashimoto, The effect of alloying elements on the corrosion behaviour of sputter-deposited amorphous Mn–Ta–Cr alloys in 1 M H2SO4, Corros. Sci. 40 (Sept. 1998) 1491–1512, https://doi.org/10.1016/S0010-938X(98)00061-4.

[59] K.A. de Souza, A. Robin, Electrochemical behavior of titanium-tantalum alloys in sulfuric acid solutions, Mater. Corros. 55 (Nov. 2004) 853–860, https://doi.org/10.1002/maco.200303792.

[60] Y.L. Zhou, M. Niinomi, T. Akahori, H. Fukui, H. Toda, Corrosion resistance and biocompatibility of Ti–Ta alloys for biomedical applications, Materials Science and Engineering: A 398 (May 2005) 28–36, https://doi.org/10.1016/j.msea.2005.03.032.

[61] F. Meng, Z. Li, X. Liu, Synthesis of tantalum thin films on titanium by plasma immersion ion implantation and deposition, Surf. Coat. Technol. 229 (Aug. 2013) 205–209, https://doi.org/10.1016/j.surfcoat.2012.04.044.

[62] M. Pourbaix, Atlas of electrochemical equilibria in aqueous solutions. No. v. 2 in Atlas of electrochemical equilibria in aqueous solutions, National Association of Corrosion Engineers, 1974.

[63] S. Permana, R. Abdul Majid, and J. Wahyuadi Soedarsono, "Hydrochloric Acid Leaching Approaches for Tantalum and Niobium Pentoxides Enrichment in 1st Tin Slag from Bangka Island," IOP Conference Series: Materials Science and Engineering, vol. 924, p. 012025, Oct. 2020. doi:10.1088/1757-899X/924/1/012025.

[64] L. Wang, J. Zhang, Y. Gao, Q. Xue, L. Hu, T. Xu, Grain size effect in corrosion behavior of electrodeposited nanocrystalline Ni coatings in alkaline solution, Scripta Mater. 55 (Oct. 2006) 657–660, https://doi.org/10.1016/j.scriptamat.2006.04.009.

[65] A. Chianpairot, G. Lothongkum, C.A. Schuh, Y. Boonyongmaneerat, Corrosion of nanocrystalline Ni–W alloys in alkaline and acidic 3.5wt.% NaCl solutions, Corros. Sci. 53 (Mar. 2011) 1066–1071, https://doi.org/10.1016/j.corsci.2010.12.001.

[66] E.V. Nikitina, V.Y. Kudyakov, V.B. Malkov, S.V. Plaksin, Corrosion-electrochemical behavior of nickel in an alkali metal carbonate melt under a chlorine-containing atmosphere, Russian Metallurgy (Metally) 2013 (Aug. 2013) 595–599, https://doi.org/10.1134/S0036029513080107.

[67] H. Holleck, Advanced concepts of PVD hard coatings, Vacuum 41 (Jan. 1990) 2220–2222, https://doi.org/10.1016/0042-207X(90)94229-J.

[68] R. Fella, H. Holleck, Preparation and properties of metastable TiC/SiC PVD coatings for wear protection, Materials Science and Engineering: A 140 (July 1991) 676–681, https://doi.org/10.1016/0921-5093(91)90495-9.

[69] S. Ulrich, H. Holleck, M. StÜer, H. Leiste, J. Ye, and C. Ziebert, "Nanocrystalline Metastable Hard Coatings," in Nanostructured Materials for Advanced Technological Applications, pp. 257–267, Dordrecht: Springer, Netherlands, 2009.

[70] K.H. Gayer, A.B. Garrett, The Equilibria of Nickel Hydroxide, Ni(OH)₂, in Solutions of Hydrochloric Acid and Sodium Hydroxide at 25, J. Am. Chem. Soc. 71 (Sept. 1949) 2973–2975, https://doi.org/10.1021/ja01177a008.

[71] D.A. Palmer, P. Bénézeth, C. Xiao, D.J. Wesolowski, L.M. Anovitz, Solubility Measurements of Crystalline NiO in Aqueous Solution as a Function of Temperature and pH, J. Solution Chem. 40 (Apr. 2011) 680–702, https://doi.org/10.1007/s10953-011-9670-x.

[72] S. Sjöberg, Silica in aqueous environments, J. Non-Cryst. Solids 196 (Mar. 1996) 51–57, https://doi.org/10.1016/0022-3093(95)00562-5.

[73] S. Chatterji, Chemistry of alkali–silica reaction and testing of aggregates, Cem. Concr. Compos. 27 (2005) 788–795, https://doi.org/10.1016/j.cemconcomp.2005.03.005.